Open Access Articles

Aspect-dependent variations in regolith creep revealed by meteoric ^{10}Be

The Faculty of Oregon State University has made this article openly available.
Please share how this access benefits you. Your story matters.

Citation	West, N., Kirby, E., Bierman, P., & Clarke, B. A. (2014). Aspect-dependent variations in regolith creep revealed by meteoric ^{10}Be. Geology, 42(6), 507-510. doi:10.1130/G35357.1
DOI	10.1130/G35357.1
Publisher	Geological Society of America
Version	Accepted Manuscript
Terms of Use	http://cdss.library.oregonstate.edu/sa-termsofuse

Publisher: GSA
Journal: GEOL: Geology
Article ID: G35357

Aspect-dependent variations in regolith creep revealed by meteoric ^{10}Be

Nicole West[1]; Eric Kirby[2]; Paul Bierman[3]; and Brian A. Clarke[1]

[1]*Department of Geosciences, Penn State University, University Park, PA 16802, USA*

[2]*College of Earth, Ocean, and Atmospheric Sciences, Oregon State University, Corvallis, OR 97331, USA*

[3]*Department of Geology and Rubenstein School of the Environment and Natural Resources, University of Vermont, Burlington, VT 05405, USA*

ABSTRACT

Although variations in insolation and emergent feedbacks among soil moisture, vegetation, and soil cohesion are commonly invoked to explain topographic asymmetry that depends on aspect, few studies have directly quantified the efficiency of regolith transport along hillslopes of opposing aspect. We utilize meteoric ^{10}Be concentrations in regolith (n = 74) to determine mass flux along equatorial- and polar-facing hillslopes in three forested, upland watersheds in and adjacent to the Susquehanna Shale Hills Critical Zone Observatory (SSHO) in central Pennsylvania. In combination with regolith depth measurements and high resolution topography, these fluxes allow us to evaluate transport rate laws and the efficiency of regolith creep. Concentrations of meteoric ^{10}Be in regolith along six separate transects imply that regolith flux is similar along all hillslopes, despite differences in topographic gradient and regolith thickness. Comparison of flux with regolith depth and topographic gradient reveals that transport depends on regolith depth, and that regolith creep is twice as efficient along low-gradient, south-facing slopes with thin regolith as compared to steep, north-facing slopes mantled with thicker

regolith. We suggest that the observed topographic asymmetry in these watersheds has evolved over geologic time as a result of differences in the frequency of freeze-thaw events between hillslopes of opposing aspect.

INTRODUCTION

Topographic asymmetry that depends on the facing direction, or aspect, of hillslopes is a common yet enigmatic characteristic of natural landscapes (e.g., Melton, 1960; Hack and Goodlett, 1960). Global analyses of topographic asymmetry suggest that equatorial-facing hillslopes are, on average, shallower than polar-facing hillslopes at mid-latitudes (Poulos et al., 2012), although deviations exist in some arid and glacial landscapes (e.g., Gilbert, 1904; Naylor and Gabet, 2007; Burnett et al., 2008). Aspect-dependent differences in hillslope angles present a challenge to models that consider transport efficiency to be uniform across landscapes (e.g., Perron et al., 2009) as they implicate potentially important feedbacks between (micro)climate and topography. In arid to semi-arid landscapes, differences in insolation are thought to lead to variations in soil moisture, vegetation, runoff processes, and effective soil cohesion (e.g., Istanbulluoglu et al., 2008) that in turn influence the efficacy of regolith creep (e.g., Pierce and Colman, 1986). Recent studies suggest that asymmetry may also evolve in alpine landscapes as a consequence of thermally-driven differences in frost shattering and creep efficiency (Anderson et al., 2013). However, no studies have directly measured mass transport rates or efficiency across asymmetric watersheds and, thus, our understanding of these phenomena remains largely inferential.

Hillslope gradients reflect the dynamic balance between relative base level fall and downslope regolith flux (e.g., Culling, 1963; Kirkby, 1971). We define regolith as the layer of chemically and physically altered material formed from weathered, but intact, parent bedrock.

The simplest description of downslope regolith flux asserts that transport is linearly proportional to the local hillslope gradient, which in one dimension is:

$$q = -K_1 \frac{dz}{dx} \quad (1)$$

where q is the volumetric regolith flux per unit width along slope [$L^2\ t^{-1}$], K_1 is analogous to a diffusion coefficient [$L^2\ t^{-1}$] describing the transport efficiency of creep processes (Culling, 1963), and dz/dx is the local hillslope gradient. Equation 1 successfully describes much of the first-order structure of landscape topography (Perron et al., 2009). Emerging evidence, however, suggests that a depth-dependent transport rule may be more appropriate for disturbance-driven regolith creep (Heimsath et al., 2005; Yoo et al., 2007; Roering, 2008; Pelletier et al., 2011). Considering that the probability of disturbance-driven regolith transport decreases with depth, a transport law, similar to Equation 1, which considers regolith flux to depend on regolith depth, local hillslope gradient, and some characteristic mixing depth, can be written as

$$q = -K_2 \left[1 - e^{-h/h^*} \left(1 + \frac{h}{h^*} \right) \right] \frac{dz}{dx} \quad (2)$$

where K_2 is a diffusion coefficient [$L^2\ t^{-1}$], h is the creeping regolith thickness [L], and h^* is the characteristic mixing depth [L] of processes driving downslope regolith creep such as freeze-thaw and/or bioturbation (e.g. Anderson, 2002). In contrast to some depth-dependent models that consider transport to be linearly dependent on the product of regolith depth and slope (e.g., Roering, 2008; Heimsath et al., 2005), this formulation acknowledges that regolith depth and the base of a mobile layer need not be coincident (Anderson, 2002).

During the past two decades, the application of meteoric ^{10}Be to the study of earth surface processes (e.g., Monaghan et al., 1992; McKean et al., 1993; Jungers et al., 2009; West et al., 2013) has allowed direct estimates of downslope regolith flux on eroding hillslopes, provided

that the delivery rate of ^{10}Be can be estimated (Willenbring and von Blanckenburg, 2010; Graly et al., 2011). Accounting for the mass balance of meteoric ^{10}Be in creeping regolith, the volumetric downslope flux (q) of regolith [cm^2/yr] can be calculated as:

$$q_x = \frac{D m_a}{C_{re} \rho_{re}} (x_0 - x) \quad (3)$$

where D is the meteoric ^{10}Be delivery rate [at/cm^2 y], m_a is the atomic mass of ^{10}Be, C_{re} is the concentration of ^{10}Be in regolith [g/g sample], ρ_{re} is the depth-averaged bulk density of regolith, and x-x_0 represents the distance between the sample location and the ridgetop (Monaghan et al., 1992; McKean et al., 1993; West et al., 2013).

In this study, we use meteoric ^{10}Be to explore the origin of asymmetric regolith-mantled hillslopes within three first-order watersheds in and adjacent to the Susquehanna Shale Hills Critical Zone Observatory (SSHO), located in central Pennsylvania. During the late Pleistocene, the terminus of the Laurentide ice sheet lay ~75 km due north, and the SSHO experienced a periglacial climate (Clark and Ciolkosz, 1988). Hillslopes in and adjacent to SSHO are characterized by convex-up ridgetops, planar mid-slopes, and concave-up toe slopes (West et al., 2013). All three watersheds have a central channel oriented approximately east-west, and all exhibit steeper north (polar)-facing hillslopes than south (equatorial)-facing hillslopes (Fig. 1). Bedding strikes at a high angle to the axis of the catchments (~50°) and dips steeply to the NW (~50°), thus, the topographic asymmetry is not a direct reflection of dipping strata. Although previous studies note this asymmetry (Ma et al., 2013; West et al., 2013), the cause of its development remains unknown.

METHODS

This work builds upon an initial study of West et al. (2013), who presented data for two hillslopes within the SSHO watershed. Our expanded data set includes 44 new meteoric ^{10}Be

measurements from four additional hillslopes (two N-facing and two S-facing); collectively, the six hillslopes span a range of average gradients from ~10° – 25° (SSHO range: 15° – 20°, Fig. 1). Regolith samples were collected with a 5 cm diameter hand auger until refusal in a 5 x 5 grid on planar hillslopes in each watershed (Fig. 1A). Sample locations were spaced ~5 m across slope and ~20 m downslope. Samples at each site were amalgamated by depth. We further mixed samples to the east and west of the central transect, so that at each position along the slope, three samples were analyzed for ^{10}Be. At the upper slope and lower slope positions, all five depth-amalgamated samples were mixed to one representative sample for those positions. Previous work showed that measured meteoric ^{10}Be inventories are not impacted by amalgamation (e.g., Jungers et al., 2009; West et al., 2013); we therefore use an amalgamation approach in this study. Using these meteoric ^{10}Be measurements, we evaluate transport rate laws and coefficients using gradients determined from a high-resolution, LiDAR-derived digital elevation model.

RESULTS

Our results reveal that regolith thickness at SSHO varies systematically with hillslope aspect (Fig. 1E, F). Along low-gradient, S-facing hillslopes, augerable regolith is relatively uniform (30 – 40 cm), with thicker (~80 cm) regolith present only at the toe of the slope. In contrast, augerable regolith is thicker (40 – 60 cm) along N-facing slopes and exhibits considerable variability in both the downslope and cross-slope directions (Fig. 1F). Observations from hand excavations and soil pits within the SSHO watershed suggest that this variability reflects the presence of a buried 1 – 1.5 m thick layer of angular colluvium on the N-facing hillside that mantles fractured bedrock (West et al., 2013). Within soil pits, we observe a distinct stratigraphy on the N-facing hillslope; massive, poorly structured regolith overlies a clast-supported framework of shale fragments up to 5 – 10 cm in diameter (Figure S1). In contrast, the

augerable, poorly structured regolith along S-facing hillslopes directly overlies weathered bedrock, and no coarse underlying colluvial material is present (Figure S1).

Meteoric ^{10}Be concentrations in regolith are similar across all hillslopes and do not vary systematically with hillslope position, amalgamation technique, or aspect (Table S1). Combining meteoric ^{10}Be concentrations with depth-averaged regolith densities and an assumed meteoric ^{10}Be delivery rate of 1.8×10^6 at/cm^{2}y (Graly et al., 2011), we estimate regolith flux (Eq. 3). Our results suggest that regolith flux increases linearly with distance from ridgecrests, and does not appear to vary with hillslope aspect (Fig. 2A). Rather, the similarity of flux patterns along sample transects appears to be consistent with spatially uniform lowering of the landscape at rates of ~20 – 30 m/My over the past 10 – 15 ka (West et al., 2013). This similarity between regolith flux along N- and S-facing hillslopes suggests that ^{10}Be is retained in the upper regolith and is not lost to deep colluvium.

To evaluate the applicability of geomorphic transport laws used to describe creeping regolith (eq. 1 and 2), we plot measured regolith flux against topographic gradient and mean regolith depth (Fig. 2). Along N-facing hillslopes, downslope regolith flux correlates with local topographic gradient (Fig. 2B), consistent with a slope-dependent transport rule (eq. 1). This correlation is poor along S-facing slopes (Fig. 2D), suggesting that such a rate law does not completely describe regolith creep. The correlation between regolith flux and a characteristic mixing depth model (eq. 2) is significantly stronger along both N- and S-facing slopes (Fig. 2C, E). Thus, our data imply that regolith flux depends on both regolith thickness and local gradient at this field site.

Our data also imply that the efficiency of creep (the coefficients K_1 and K_2), varies among hillslopes of opposing aspect (Fig. 2). Assuming a characteristic mixing depth of 100 cm,

consistent with the depth of root and frost penetration (Gaines et al., 2013; NSIDC, 2013), the diffusion coefficient K_2 on N-facing slopes ranges from ~46 – 98 cm^2/yr (Fig. 2C), whereas K_2 values on S-facing slopes are nearly twice as high, ranging from 81– 187 cm^2/yr (Fig. 2E). This difference is also apparent in the linear transport model; K_1 varies from 27 – 56 cm^2/y on N-facing slopes but from 60 – 123 cm^2/y on S-facing slopes (Fig. 2B, D). Moreover, the difference in transport efficiency between hillslopes of opposing aspect is greater than variability in transport efficiency among hillslopes of similar aspect (Fig. 2B-E). That the apparent asymmetry in transport efficiency does not depend on the form of the transport rule suggests the difference in efficiency between polar- and equatorial-facing slopes is a robust result of our study.

DISCUSSION

Several lines of evidence suggest that the deep colluvial material along the N-facing slope of SSHO does not presently participate in downslope creep or in the transport of meteoric ^{10}Be. First, the rooting depth of large woody vegetation (Gaines et al., 2013) and the scale of pit-and-mound topography associated with tree throw events appear to be on the order of ~1 m, near the top of the buried immobile colluvium. Similarly, average freezing depths reach ~1 m in central Pennsylvania (NSIDC, 2013), suggesting freeze-thaw does not presently activate motion in the buried colluvium. Additionally, the colluvial mantle itself retains a crude clast alignment reminiscent of structure in periglacial deposits (e.g., *grèzes litées*). Finally, meteoric ^{10}Be data from S-facing hillslopes, where the depth to refusal directly coincides with the boundary between disaggregated regolith and mechanically intact (but fractured) rock, yields identical fluxes as those along N-facing hillsides suggesting that these data capture most, if not all, of the mobile regolith transport.

The observation that regolith flux is equivalent on N- and S-facing slopes despite systematic differences in regolith depth and topographic gradient on opposing hillslopes provides quantitative evidence that microclimate variations associated with hillslope aspect influence the efficiency of regolith transport on soil mantled hillsides. Although the total regolith flux from N- and S-facing hillslopes in our studied watersheds is equivalent within uncertainty (Fig. 2A), the differences in gradient and regolith depth along these hillslopes require more efficient regolith transport on S-facing hillslopes. In all three watersheds, the transport coefficient (K_1 or K_2) is approximately a factor of two greater along the S- (equatorial-) facing hillslopes than along the N- (polar-facing) slopes (Fig. 2B-E).

Our tests of transport rules at SSHO suggests that considering the probability distribution of disturbance with regolith depth (e.g., Anderson, 2002; Anderson 2013) provides a better characterization of regolith transport and erosion on hillslopes than a first-order rate law that depends solely on gradient. Our study thus bolsters a growing body of evidence in support of rules that incorporate regolith depth and/or velocity gradients into landscape evolution models (e.g., Heimsath et al., 2005; Pelletier et al., 2011).

Tree species, tree density, and rooting depths are similar across the watershed (Gaines et al., 2013), suggesting no difference in bioturbation on N- and S-facing slopes. However, heave during freeze-thaw cycles may be controlled by aspect at SSHO. Variations in stable isotope ratios in modern soil waters at the SSHO suggest enhanced snow-melt and infiltration on S-facing hillslopes (Thomas et al., 2013), as regolith on N-facing hillslopes remains frozen and shielded under snow pack for a greater fraction of the winter. Thus, these proxy data suggest the possibility that greater insolation on the S-facing hillslopes is associated with more frequent freeze-thaw and wetting-drying events. Because these processes are associated with slope-

normal volumetric expansion and gravitational collapse of regolith that drive downslope creep (e.g., Anderson et al., 2013), we suggest that they provide a ready explanation for both the depth-dependence of regolith transport and the variability in transport efficiency.

If we further consider that transport largely occurs during frost heave, we can relate transport to the contribution of freeze-thaw events. In this case, the transport efficiency of frost heave reflects the frequency and magnitude of freeze-thaw events, and K_2 is then transformed to

$$K_2 = \frac{1}{2} f \beta h^{*2} \quad (4)$$

where f is the frequency of freezing events (t^{-1}), β is the strain associated with regolith expansion during freezing, and h^* is the maximum frost penetration depth (Anderson, 2002). Assuming that frost penetration depth and freezing strain do not change with aspect, freeze-thaw events must be twice as frequent on S-facing hillslopes than N-facing hillslopes at SSHO in order to account for the differences in transport efficiency. Therefore, the transport efficiencies observed at SSHO suggest freeze-thaw frequencies of 0.1 – 0.2 y^{-1} for N-facing slopes and 0.2 – 0.4 y^{-1} for S-facing slopes. These values are consistent with modeled return periods of frost penetration to 100 cm in bare soil (no snow) for central Pennsylvania (DeGaetano et al., 1996).

Finally, the asymmetric topography in our study area suggests that the difference in transport efficiency has been sustained over geologic time. The location of the SSHO in the mid-latitudes, where annual fluctuations in temperature allow freeze-thaw processes to be relatively efficient, and the slow erosion and lowering of the Appalachian landscapes (Portenga et al., 2013), appear to have conspired to allow microclimatic differences to be expressed in topography (e.g., Poulos et al., 2012). The proximity to the terminus of the Laurentide ice sheet would have enhanced frost-heave mediated transport during Pleistocene climate variations, potentially setting the stage for the modern observed aspect-related topographic asymmetry. Our

data imply that topographic asymmetry observed at SSHO, and perhaps elsewhere in the mid-latitudes, represents an equilibrium solution to aspect-related microclimate differences even under conditions of uniform lowering and erosion over geologic time.

ACKNOWLEDGMENTS

We thank A. Neely and C. Regalla for field assistance and B. DeJong for ^{10}Be extraction, and R. Anderson, A. Heimsath, and two anonymous reviewers. Work supported by the NSF CZO program (EAR 07-25019, EAR 12-39285). NW acknowledges support from a NASA Earth and Space Science Fellowship (NNX11AL72H).

REFERENCES CITED

Anderson, R.S., 2002, Modeling of tor-dotted crests, bedrock edges and parabolic profiles of the high alpine surfaces of the Wind River Range, Wyoming, Geomorphology, v. 46, p. 35–58.

Anderson, R.S., Anderson, S.P., and Tucker, G.E., 2013, Rock damage and regolith transport by frost: An example of climate modulation of the geomorphology of the critical zone: Earth Surface Processes and Landforms, v. 38, p. 299–316, doi:10.1002/esp.3330.

Burnett, B.N., Meyer, G.A., and McFadden, L.D., 2008, Aspect-related microclimatic influences on slope forms and processes, northeastern Arizona: Journal of Geophysical Research, v. 113, F03002, doi:10.1029/2007JF000789.

Clark, G.M., and Ciolkosz, E.J., 1988, Periglacial geomorphology of the Appalachian highlands and interior highlands south of the glacial border – A review: Geomorphology, v. 1, p. 191–220, doi:10.1016/0169-555X(88)90014-1.

Culling, W.E.H., 1963, Soil creep and the development of hillside slopes: The Journal of Geology, v. 71, p. 127–161, doi:10.1086/626891.

DeGaetano, A.T., Wilks, D.S., McKay, M., 1996, Atlas of Soil Freezing Depth Extremes for the Northeastern United States, Northeastern Regional Climate Center Research Series, Publication No. RR 96-1.

Gaines, K.P., Eissenstat, D., Lin, H., 2013, Patterns in tree water extraction depth at the Susquehanna Shale Hills Critical Zone Observatory in central Pennsylvania, ESA Annual Meeting, Minneapolis, Minnesota, August 4-9, 2013.

Gilbert, G.K., 1904, Systematic Asymmetry of Crest Lines in the High Sierra of California, Journal of Geology, v. 127, p. 579–588.

Graly, J.A., Reusser, L.J., and Bierman, P.R., 2011, Short and long-term delivery rates of meteoric ^{10}Be to terrestrial soils: Earth and Planetary Science Letters, v. 302, p. 329–336, doi:10.1016/j.epsl.2010.12.020.

Hack, J.T., and Goodlett, J.C., 1960, Geomorphology and Forest Ecology of a mountain region in the central Appalachians: Geological Survey Professional Paper 343, 66 p.

Heimsath, A.M., Furbish, D.J., and Dietrich, W.E., 2005, The illusion of diffusion: Field evidence for depth dependent sediment transport: Geology, v. 33, p. 949–952, doi:10.1130/G21868.1.

Istanbulluoglu, E., Yetemen, O., Vivoni, E.R., Gutiérrez-Jurado, H.A., and Bras, R.L., 2008, Eco-geomorphic implications of hillslope aspect: Inferences from analysis of landscape morphology in central New Mexico: Geophysical Research Letters, v. 35, L14403, doi:10.1029/2008GL034477.

Jungers, M.C., Bierman, P.R., Matmon, A., Nichols, K., Larsen, J., and Finkel, R., 2009, Tracing hillslope sediment production and transport with in situ and meteoric ^{10}Be: Journal of Geophysical Research, v. 114, doi:10.1029/2008JF001086.

Kirkby, M.J., 1971, Hillslope process-response models based on the continuity equation: Institute of British Geographers Special Publication, v. 3, p. 15–30.

Ma, L., F. Chabaux, West, N., Kirby, E., Jin, L., Brantley, S., 2013, Regolith production and transport in the Susquehanna Shale Hills Critical Zone Observatory, Part 1: Insights from U-series isotopes, Journal of Geophysical Research, v. 118, p. 722–740, doi:10.1002/jgrf.20037.

McKean, J.A., Dietrich, W.E., Finkel, R.C., Southon, J.R., and Caffee, M.W., 1993, Quantification of soil production and downslope creep rates from cosmogenic ^{10}Be accumulations on a hillslope profile: Geology, v. 21, p. 343–346, doi:10.1130/0091-7613(1993)021<0343:QOSPAD>2.3.CO;2.

Melton, M.A., 1960, Intravalley variation in slope angles related to microclimate and erosional environment: Geological Society of America Bulletin, v. 71, p. 133–144, doi:10.1130/0016-7606(1960)71[133:IVISAR]2.0.CO;2.

Monaghan, M.C., McKean, J., Dietrich, W., and Klein, J., 1992, ^{10}Be chronometry of bedrock-to-soil conversion rates: Earth and Planetary Science Letters, v. 111, p. 483–492, doi:10.1016/0012-821X(92)90198-5.

Naylor, S., Gabet, E.J., 2007, Valley asymmetry and glacial versus nonglacial erosion in the Bitterroot Range, Montana, USA, Geology, v. 354, p. 375–378, doi: 10.1130/G23283A.1

National Snow and Ice Data Center, 2013, nsidc.org (September 2013).

Pelletier, J.D., McGuire, L.A., Ash, J.L., Engelder, T.M., Hill, L.E., Leroy, K.W., Orem, C.A., Rosenthal, W.S., Trees, M.A., Rasmussen, C., and Chorover, J., 2011, Calibration and testing of upland hillslope evolution models in a dated landscape: Banco Bonito, New Mexico: Journal of Geophysical Research, v. 116, doi:10.1029/2011JF001976.

Perron, J.T., Kirchner, J.W., and Dietrich, W.E., 2009, Formation of evenly spaced ridges and valleys: Nature, v. 460, p. 502–505, doi:10.1038/nature08174.

Pierce, K.L., and Colman, S.M., 1986, Effect of height and orientation (microclimate) on geomorphic degradation rates and processes, late glacial terrace scarps in central Idaho: Geological Society of America Bulletin, v. 97, p. 869–885, doi:10.1130/0016-7606(1986)97<869:EOHAOM>2.0.CO;2.

Portenga, E.W., Bierman, P.R., Rizzo, D.M., and Rood, D.H., 2013, Low rates of bedrock outcrop erosion in the central Appalachian Mountains inferred from in situ ^{10}Be: Geological Society of America Bulletin, v. 125, p. 201–215, doi:10.1130/B30559.1.

Poulos, M.J., Pierce, J.L., Flores, A.N., and Benner, S.G., 2012, Hillslope asymmetry maps reveal widespread, multi-scale organization: Geophysical Research Letters, v. 39, L06406, doi:10.1029/2012GL051283.

Roering, J.J., 2008, How well can hillslope evolution models “explain” topography? Simulating soil transport and production with high-resolution topographic data: Geological Society of America Bulletin, v. 120, p. 1248–1262, doi:10.1130/B26283.1.

Thomas, E.M., Lin, H., Duffy, C.J., Sullivan, P.L., Holmes, G.H., Brantley, S.L., and Jin, L., 2013, Spatiotemporal patterns of water stable isotope compositions at the Shale Hills Critical Zone Observatory: Linkages to subsurface hydrologic processes: Vadose Zone Journal, doi:10.2136/vzj2013.01.0029.

West, N., Kirby, E., Bierman, P., Slingerland, R., Ma, L., Rood, D., and Brantley, S., 2013, Regolith production and transport at the Susquehanna Shale Hills Critical Zone Observatory, Part 2: Insights from meteoric ^{10}Be: Journal of Geophysical Research, doi:10.1002/jgrf.20121.

Willenbring, J.K., and von Blanckenburg, F., 2010, Meteoric cosmogenic Beryllium-10 adsorbed to river sediment and soil: Applications for Earth-surface dynamics: Earth-Science Reviews, v. 98, p. 105–122, doi:10.1016/j.earscirev.2009.10.008.

Yoo, K., Amundson, R., Heimsath, A.J., Dietrich, W.E., and Brimhall, G.H., 2007, Integration of geochemical mass balance with sediment transport to calculate rates of soil chemical weathering and transport on hillslopes: Journal of Geophysical Research, v. 112, F02013, doi:10.1029/2005JF000402.

FIGURE CAPTIONS

Figure 1. A) Topographic gradient of watersheds in and adjacent to SSHO. Histograms show the distribution of gradient from the sampled regions of planar hillslopes (solid black boxes) along the N-facing (orange) and S-facing (blue) hillslopes in NV1, SSHO and SV1 (B, C and D, respectively). E) Depth to refusal for hand auger along S-facing (open symbols) and F) N-facing hillslopes (closed symbols) for NV1, SSHO and SV1. Error bars in A and B represent one standard deviation of the mean auger depth at each position.

Figure 2. A) Scatter plots of regolith flux with distance from the ridge crest. Error bars represent one standard deviation from the mean flux at each position. Regolith flux increases linearly with position downslope in all 3 watersheds and is similar between N-facing (closed symbols) and S-facing (open symbols) hillslopes. Regression line passes through zero at the ridgecrest where flux sums to zero. B and C) Scatter plots of regolith flux with slope and the product of slope and transport profile for N-facing and D, E) S-facing hillslopes. A transport rule that considers regolith depth is a better predictor of measured regolith flux on all hillslopes. Variations in the slope of linear regressions show that transport efficiencies are consistently a factor of two higher on S-facing hillslopes.

[1]GSA Data Repository item 2014xxx, xxxxxxxx, is available online at www.geosociety.org/pubs/ft2014.htm, or on request from editing@geosociety.org or Documents Secretary, GSA, P.O. Box 9140, Boulder, CO 80301, USA.

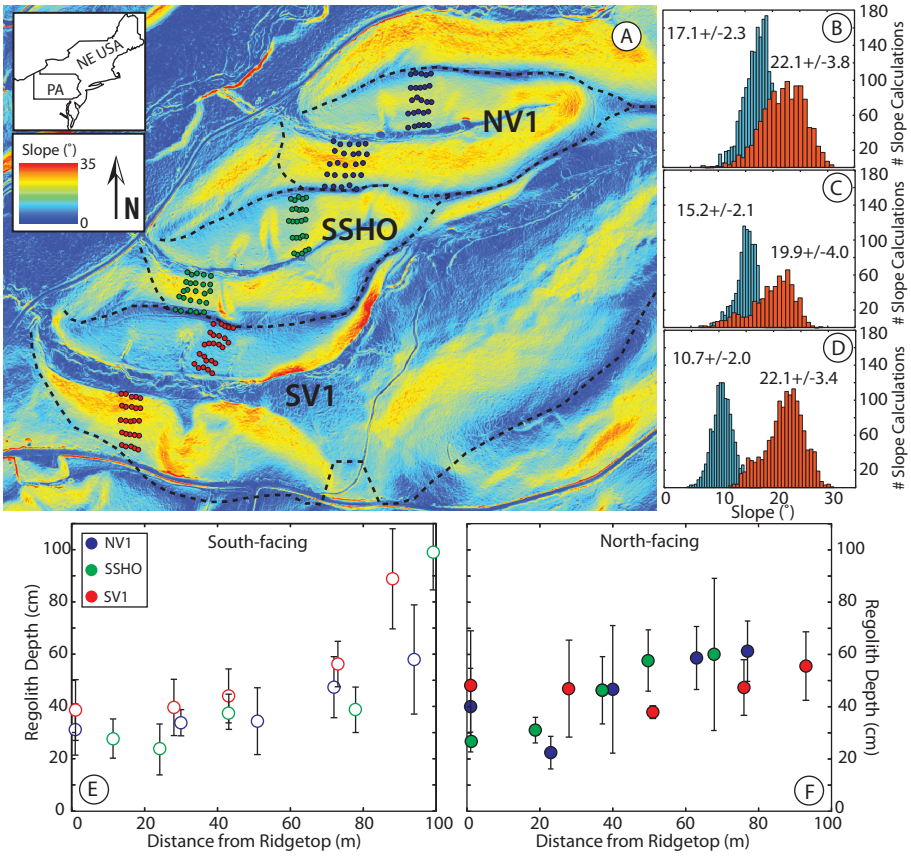

West_et_al_2014_Figure1

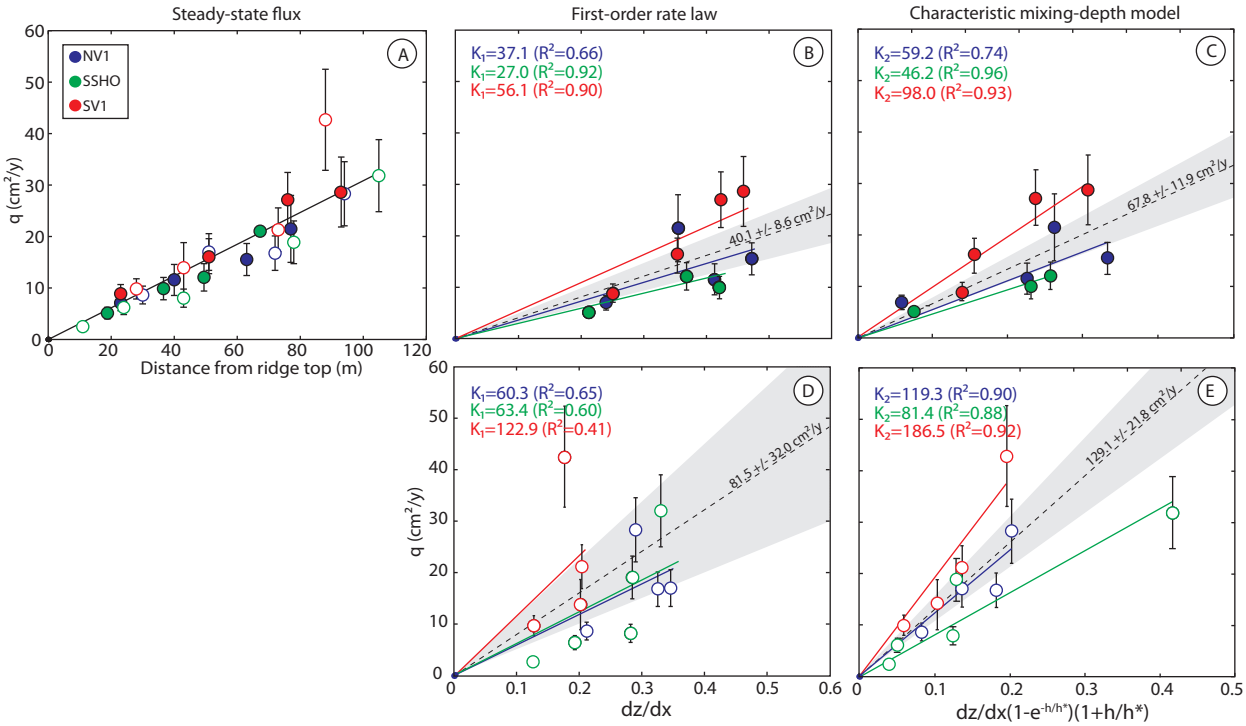

West_et_al_2014_Figure2

SUPPLEMENTAL INFORMATION

Sampling and Analytical Methods

Meteoric ^{10}Be

Regolith samples were collected with a 5 cm diameter hand auger until refusal in a 5 x 5 grid on a representative, planar north- and south-facing hillslope in each watershed (Figure S1). Sample locations were spaced ~ 5 m in the cross-slope direction and ~ 20 m in the downslope direction (Figure S1). For sample locations along the center line of the grid, regolith was sampled at 10 cm intervals throughout the entire augerable thickness. Using a Riffle splitter, 1/8 splits from each aliquot were amalgamated in the lab to a single depth-averaged sample for each hillslope position. This approach was tested by West and others (2013) who showed that meteoric ^{10}Be inventories calculated using individual aliquots from depth profiles were equivalent to physically amalgamated samples. At all other sample locations, the entire thickness of augerable material was amalgamated in the field to one representative depth-averaged sample for each location.

Our previous work at SSHO demonstrated that meteoric ^{10}Be depth profiles are characteristic of addition from the surface by precipitation and dry-fall; concentrations of ^{10}Be are highest at the surface and decline to the depth of auger refusal (West et al., 2013). Moreover, ^{10}Be inventories in the upper decimeters of a bedrock core were < 10 – 15 % of regolith inventories, suggesting effective sequestering of ^{10}Be in clay-rich regolith. Total measured meteoric ^{10}Be inventories in depth profiles were similar to average samples of bulk regolith and to amalgamated samples along cross-hillslope transects (West et al., 2013). Guided by these results, we use an amalgamated sampling approach along the four additional hillslopes to determine mean ^{10}Be concentrations (Figure S1).

For meteoric ^{10}Be analyses, the depth-amalgamated samples from the center ridgetop (RT), midslope (MS), and valley floor (VF) of each hillslope were analyzed as individual samples (Figure S1). Again, using a Riffle splitter, 1/8 splits of each field-amalgamated sample to the east and west of the center samples were mixed (the 2 samples to east were mixed and the 2 samples to west were mixed), producing 3 analytical samples for each RT, MS, and VF position. At positions between the RT and MS and VF positions (US and LS, respectively), 1/8 splits from all 5 collected samples were amalgamated, producing one representative sample for analysis at each position, totaling 11 analyzed samples per hillslope.

Sample preparation and analytical techniques used in this study are described in detail in West et al. (2013). However, beryl-derived ^{9}Be carrier was used during ^{10}Be extractions from samples collected from the watersheds adjacent to SSHO, and a second precipitation step was completed out of nitric acid after cation columns were used to remove boron, an isobar of ^{10}Be. ^{10}Be/^{9}Be ratios were measured at the Center for Accelerator Mass Spectrometry, Lawrence Livermore National Lab and normalized to standard 07KNSTD3110 with a reported ^{10}Be/^{9}Be ratio of 2850×10^{-15} (Nishiizumi et al., 2007). Meteoric ^{10}Be concentrations measured in this study are listed in Table S1.

SUPPLEMENTAL FIGURE CAPTIONS

Figure S1. Sample and amalgamation strategy for hillslopes adjacent to SSHO. Open symbols indicate locations of samples collected in 10 cm intervals. 1/8 splits of these aliquots were mixed for a depth-amalgamated sample at each location. Closed symbols indicate samples that were mixed in the field; the entire augerable thickness was collected as one sample for each

location. 1/8 splits of samples within bounding boxes were amalgamated to one analytical sample per box, resulting in 11 meteoric ^{10}Be analyses per hillslope.

Figure S2. Photographs of soil pits excavated at mid-slope positions on the south-facing (A) and north-facing (B) hillslopes of SSHO. Regolith directly overlies bedrock on the south-facing hillslope of SSHO. On the north-facing hillslope of SSHO, augerable regolith overlies a thick colluvial layer comprised of large, interlocking shale clasts. Red lines show the approximate depths to hand auger refusal. Pictured hammer is ~ 35 cm tall.

SUPPLEMENTAL REFERENCES CITED

Nishiizumi, K., M. Imamura, M.W. Caffee, J.R. Southon, R.C. Finkel, J. McAninch (2007), Absolute calibration of ^{10}Be standards, *Nucl. Instrum.Meth. Phys. Res. B, 258*, 403 – 413.

West, N., E. Kirby, P. Bierman, R. Slingerland, L. Ma, D. Rood, S. Brantley (2013) Regolith production and transport at the Susquehanna Shale Hills Critical Zone Observatory, Part 2: Insights from meteoric ^{10}Be, *Journal of Geophysical Research*, doi: 10.1002/jgrf.20121.

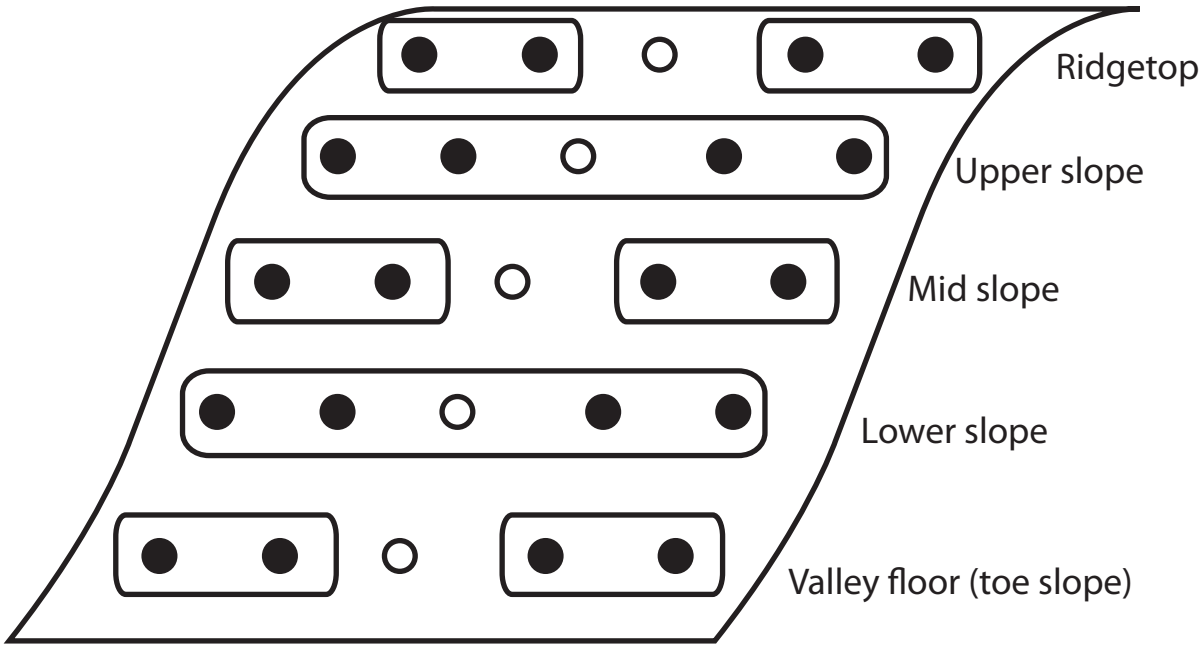
Ridgetop
Upper slope
Mid slope
Lower slope
Valley floor (toe slope)

South-facing

North-facing

Westetal_SupplementalFigureS2.ai

Table S2. Measured flux, hillslope gradient, and regolith thickness

Hillslope position	Flux (cm^2/y)	slope	mean regolith depth (cm)
NV1NPRT	0	0	31
NV1NPUS	8.63	0.21	33.8
NV1NPMS	16.99	0.35	34.4
NV1NPLS	16.76	0.33	47.4
NV1NPLS	28.31	0.29	58
NV1SPRT	0	0	39.8
NV1SPUS	6.98	0.24	22.4
NV1SPMS	11.56	0.41	46.6
NV1SPLS	15.53	0.47	58.6
NV1SPVF	21.48	0.35	61.2
SV1NPRT	0	0	38.7
SV1NPUS	9.82	0.13	39.6
SV1NPMS	13.94	0.2	44
SV1NPLS	21.31	0.2	56.2
SV1NPVF	42.68	0.18	88.8
SV1SPRT	0	0	45.7
SV1SPUS	8.88	0.25	47
SV1SPMS	16.17	0.36	38
SV1SPLS	27.04	0.42	47.4
SV1SPVF	28.65	0.46	55.6

Flux, slope and depth values for SSHO are found in West et al. (2013)